Near-Field Imaging of Free Carriers in ZnO Nanowires with a Scanning Probe Tip made of Heavily Doped Germanium

Emilie Sakat[1,2], Valeria Giliberti[3,4], Monica Bollani[5], Andrea Notargiacomo[5], Marialilia Pea[5], Marco Finazzi[1], Giovanni Pellegrini[1], Jean-Paul Hugonin[2], Alexander Weber-Bargioni[6], Mauro Melli[6], Simone Sassolini[6], Stefano Cabrini[6], Paolo Biagioni[1,5], Michele Ortolani[3,4,5,*] and Leonetta Baldassarre[3,4]

[1] *Dipartimento di Fisica, Politecnico di Milano, Piazza Leonardo da Vinci 32, I-20133 Milan, Italy*

[2] *Laboratoire Charles Fabry, Institut d'Optique Graduate School, CNRS, Université Paris-Saclay, 91127 Palaiseau, France*

[3] *Dipartimento di Fisica, Sapienza Università di Roma, Piazzale Aldo Moro 5, I-00185 Rome, Italy*

[4] *Istituto Italiano di Tecnologia, Center for Life NanoSciences, Viale Regine Elena 291, I-00185 Rome, Italy*

[5] *Istituto di Fotonica e Nanotecnologie, Consiglio Nazionale delle Ricerche, P. Leonardo da Vinci 32, 20133, Milan, Italy*

[6] *Molecular Foundry, Lawrence Berkeley National Laboratory, Berkeley CA 94720, U.S.A.*

Corresponding author e-mail: michele.ortolani@roma1.infn.it

Abstract. *A novel scanning probe tip made of heavily doped semiconductor is fabricated and used instead of standard gold-coated tips in infrared scattering-type near-field microscopy. Mid-infrared near-field microscopy experiments were conducted on ZnO nanowires with a lateral resolution better than 100 nm, using tips made of heavily electron-doped germanium with plasma frequency in the mid-infrared (plasma wavelength of 9.5 μm). Nanowires embedded in a dielectric matrix were imaged at two wavelengths, 11.3 μm and 8.0 μm, above and below the plasma wavelength of the tips. An opposite sign of the imaging contrasts between the nanowire and the dielectric matrix was observed at the two infrared wavelengths, indicating a clear role of the free electron plasma in the heavily doped germanium tip in building the imaging contrast. Electromagnetic simulations with a multi-spherical dipole model accounting for the finite size of the tip are well consistent with the experiments. By comparison of the simulated and measured imaging contrasts, an estimate for the local free carrier density in the investigated ZnO nanowires in the low 10^{19} cm^{-3} range is retrieved. The results are benchmarked against the scattering intensity and phase maps obtained on the same sample with a gold-coated probe tip in pseudo-heterodyne detection mode.*

Keywords: near-field microscopy, infrared nanoimaging, plasmonics, focused ion beam, scanning probe fabrication, doped semiconductor nanowires.

In the last decade, scattering-type Scanning Near Field Optical Microscopy (s-SNOM) [1,2], also called apertureless SNOM, has arisen as one of the most powerful techniques for material characterization at the nanoscale [3] with deeply sub-λ resolution of a few tens of nanometers [4-9], enabling mid-infrared (mid-IR) spectroscopy (typically in the

wavelength range 5 μm < λ < 15 μm), and non-contact measure of the electrical conductivity of nanoobjects [10,11]. When applied to the study of nanowires (NW), s-SNOM has mostly been used to estimate the local free charge-carrier density N, a quantity of great importance in NW applications [12-14] that is extremely difficult to predict before NW growth [15] or to estimate from electrical or thermal transport measurements on nanodevices featuring metal contacts and junctions [16-19]. Due to its deeply sub-λ resolution, s-SNOM can even provide spatial profiles of N in single NWs by nanospectroscopic detection of the scattering resonance of the free carrier plasma [6, 10, 11], whose amplitude and frequency are both proportional to $\sqrt{N/m^*}$, m^* being the carrier effective mass. For high N values of the order of 10^{19} cm^{-3}, and for small-m^* semiconductor NWs like electron-doped InP ($m^* = 0.08\ m_e$, where m_e is the bare electron mass) or GaAs ($m^* = 0.067\ m_e$), the scattering resonance of the free carrier plasma typically sits in the mid-IR range. In some important NW systems, e.g. ZnO NWs [11, 14, 15] now employed as nanolasers [20, 21] and piezoelectric nanogenerators [22], however, the plasma resonance is not very evident in the s-SNOM intensity spectra [11], either because the carrier relaxation time is very short [23] and, consequently, the intrinsic resonance lineshape is too broad [24], or because N is inhomogeneous over length scales smaller than the typical lateral resolution of s-SNOM [11], leading to extrinsic plasma resonance broadening. In electron-doped ZnO, moreover, $m^* = 0.29\ m_e$, [24] which is a rather large value that leads to a weak plasma resonance and/or to a plasma frequency falling outside the typical s-SNOM measurement range. Measurement of the phase and amplitude of the s-SNOM signal provides higher sensitivity than simple intensity measurements [10-11], but this requires the pseudo-heterodyne detection mode and a longer acquisition time per pixel [25, 26]. Following the lines of Refs. 25 and 26, it would be highly desirable to implement a new practical version of homodyne s-SNOM that can be used to get at least estimates of N in NWs made of ZnO and other materials not displaying sharp plasma resonances in the mid-IR. To this aim, we introduce here a new type of probe tips heavily-doped semiconductor featuring their own plasma resonance in the mid-IR [27].

In previous s-SNOM experiments aimed at determining N in semiconductors, gold-coated pyramidal probe tips were used and broad IR frequency intervals were required for nanospectroscopy. For example, in Ref. 4 both terahertz and mid-IR data obtained with different laser systems were combined to measure N in silicon transistors in the 10^{18} - 10^{20} cm^{-3} range, while in Ref. 10 several mid-IR tunable lasers were employed to measure N in InP nanowires in the 10^{19} - 10^{20} cm^{-3} range by detecting the NW plasma resonance. More recently, both ultra-broadband IR synchrotron radiation [5,7] and IR supercontinuum radiation generated by femtosecond lasers [6,8] were coupled to s-SNOM systems to study the electrodynamic response of nanocrystals and nanowires. In general, in a broadband spectroscopy approach to s-SNOM, the tip is located at a few positions within the sample to acquire IR spectra and detect sample resonances therein [5-10]. In this case, the broadband spectrum typically displayed by pyramidal gold-coated probe tips [28], which lack sharp electromagnetic resonances, is a positive feature if one aims at unambiguously identifying the

resonance(s) belonging to the sample. In the present work, instead of broadband gold-coated tips, we employ engineered probe tips made of heavily electron-doped germanium (n-Ge) with plasma frequency in the mid-IR [27, 29, 30], with the aim of estimating *N* in NWs that do not display a clear plasma resonance. The scattering intensity maps are recorded at two IR frequencies, one above and one below the plasma frequency of the engineered n-Ge tip, which then features either a negative or a positive dielectric permittivity. The comparison of the two maps with an electromagnetic model based on the optical properties of the tip, precisely measured on the high crystal-quality epitaxial n-Ge material before probe fabrication, allows for an estimate of *N* in a ZnO NW sample (N_{ZnO}) and for free carrier density profiling along the NWs. The estimate and the profile are benchmarked against those obtained from phase and amplitude measurements on the same NWs with a conventional gold-coated monolithic probe tip in the pseudo-heterodyne detection mode, and they are found to be in good agreement.

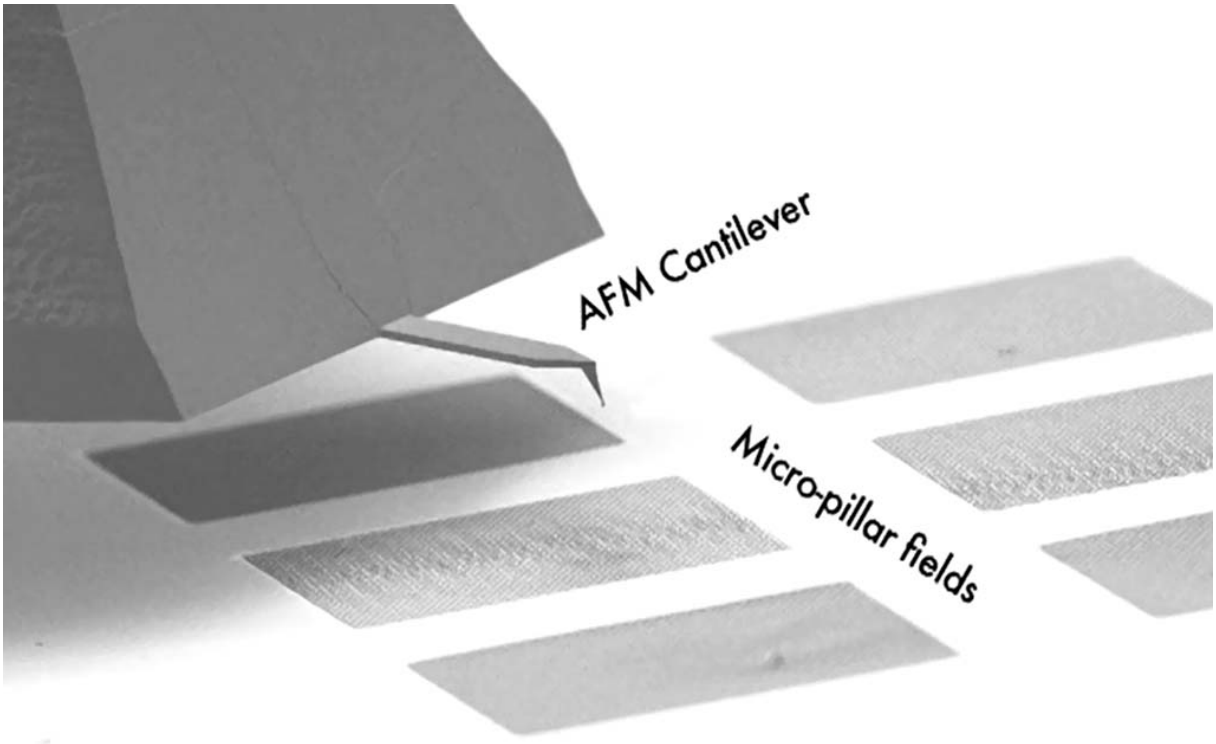

VIDEO 1. Nanofabrication process of the n-Ge tip. The n-Ge epitaxial layer grown on a Si wafer is first patterned into micro-pillars. The extremity of an AFM cantilever probe, with the tip apex intentionally removed by focused ion beam milling, is placed in contact with the top surface of one of the micro-pillars. The probe is glued to the pillar by electron-beam induced deposition of a platinum/carbon composite. The pillar base is subsequently cut by ion milling and the n-Ge epitaxial layers are detached from the Si wafer using the silicon cantilever itself as a manipulation probe. Finally, the n-Ge layer is shaped into a four-side pyramid with curvature radius of about 50 nm [27].

RESULTS AND DISCUSSION

The presentation of the results starts from a description of the engineered doped semiconductor probe, including the experimentally determined response function of the material and electromagnetic simulations of the tip. Then, a

scattering near-field microscopy experiment on a ZnO nanowire is presented and it is compared to electromagnetic models, with the aim of determining a range of values for the free charge carrier density in the nanowire.

Doped semiconductor tip engineering. Sophisticated probe tips have been engineered for a variety of different purposes [28, 31-34]: for instance, gold-coated cones [31] and pyramids [32] have been attached to cantilevers and used as scanning resonant antennas for s-SNOM microscopy, while gold nanorods with engineered length and shape have been employed to perform s-SNOM molecular vibrational nanospectroscopy [28]. To realize the probe employed in this work, we have first attached n-Ge layer blocks to silicon cantilevers to be used for s-SNOM, and then we have nano-sculptured pyramidal tips by focused ion beam milling [35]. The s-SNOM probe engineering technique is presented in Video 1. In the mid-IR range, n-Ge displays no interband optical transitions (like many other electron-doped semiconductors [8]) hence it approximately behaves as an ideal Fermi liquid [29], with complex dielectric function written according to the Drude model as:

$$\tilde{\varepsilon}_{tip}(\omega) = \varepsilon'_{tip} + i\,\varepsilon''_{tip} = \varepsilon_\infty\left(1 - \frac{\omega_p^2}{\gamma^2+\omega^2}\right) + i\frac{1}{\omega}\left(\frac{\varepsilon_\infty\omega_p^2\gamma}{\gamma^2+\omega^2}\right), \qquad (1)$$

where ω_p is the (screened) plasma frequency of the tip, ε_∞ is the dielectric screening constant due to valence electrons oscillating at higher frequencies, and $\gamma \ll \omega_p$ is the electron energy relaxation rate. In Equation 1, one sees that a crossover exists from a negative permittivity $\varepsilon'_{tip} < 0$ at frequency $\omega < \omega_p$, to a positive permittivity $\varepsilon'_{tip} > 0$ at $\omega > \omega_p$. In the mid-IR below ω_p, a doped semiconductor displays a very small negative value of ε'_{tip} and an intrinsic spheroid-polarizability resonance is established [30] , at odds with wire-like resonances of mid-IR antennas made of noble metals with ω_p in the visible range [28, 33, 34, 36], for which the wire length determines the resonance frequency. Given the present-day n-Ge thin-film growth technology, tips with any value of ω_p up to ≈ 3000 cm^{-1} could be engineered and adapted to specific s-SNOM experiments. In Figure 1a we plot the complex dielectric function of the specific n-Ge material used in this work for s-SNOM probe engineering, which displays ω_p = 1050 cm^{-1} and is well described by the Drude model (dashed lines). From the data in Figure 1a the complex polarizability of a n-Ge sphere of radius $r \approx 50$ nm, approximating the tip apex, is calculated in the quasistatic limit as $\tilde{\alpha} = 4\pi r^3(\tilde{\varepsilon}_{tip} - 1)/(\tilde{\varepsilon}_{tip} + 2)$ and it displays a maximum in its absolute value just below ω_p accompanied by a phase-delay peak exceeding $\pi/4$ (see Figure 1b).

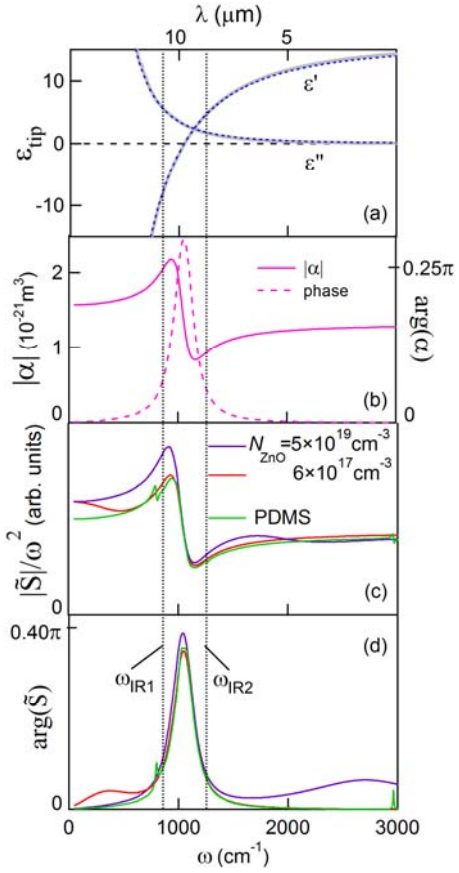

FIGURE 1. Image point-dipole model. (a) Dielectric function of the epitaxial electron-doped germanium film used in this work for scanning probe tip engineering. Grey thick lines: IR experiment[27], dashed lines: Drude fit with ω_p=1050 cm^{-1}, γ=205 cm^{-1}, ε_∞ = 16.0. (b) Polarizability amplitude and phase of a sphere of radius r = 50 nm made of n-Ge. (c) Scattering amplitude and (d) phase of the n-Ge sphere when positioned 10 nm from a semi-infinite plane made of ZnO, calculated in the framework of the image dipole model. Two carrier density values have been considered for ZnO: N_{ZnO} = 5×10^{19} cm^{-3} ("good" conductor, purple curves) and N_{ZnO} = 6×10^{17} cm^{-3} ("bad" conductor, red curves). The scattering amplitude is also calculated for a semi-infinite plane made of the dielectric matrix material used in this work (PDMS, green curve, almost overlapping with the one of the "bad" ZnO conductor, red curve). For PDMS we use a multi-Lorentzian model with ε_∞ = 2.0. For ZnO we use ε_∞ = 3.7, γ=600/1500 cm^{-1} for the red/purple curve, and m^*=0.29 m_e. The amplitude contrast between good and bad conductors around 900 cm^{-1} is exploited in this work for s-SNOM imaging. The two vertical dotted lines mark the two measurement frequencies ω_{IR1} and ω_{IR2}.

We now consider the behavior of a doped semiconductor tip for s-SNOM on both a high-N and a low-N ZnO sample surface. To do this, we use the image point-dipole (IPD) model, in which the tip is considered as a small spherical dipole inducing an image dipole in a semi-infinite homogeneous sample plane [1, 37]. The sample optical properties were chosen to reproduce those of ZnO with very high N and very low N, in both cases with short Drude relaxation time of 0.02 ps [23, 24] (for comparison, the relaxation time of the InP NW of Ref. 10 is 1.0 ps). The moduli of the calculated scattering cross-sections of the tip-surface image-dipole system strongly increase below ω_p and then fall abruptly above ω_p (see continuous curves in Figure 1c). The scattering phases have a sharp peak at ω_p approaching $\pi/2$ (dashed curves in Figure 1c). This behavior of the scattering functions mirrors the ones already observed by s-SNOM on NW samples, however we remark that the plasma resonance here belongs to the tip and not to the sample. Importantly for the aim of the present work, the sharp features seen in the scattering cross-sections for a high-N_{ZnO} sample in Figure 1c (purple curves) decrease in strength with decreasing N_{ZnO} (red curves), and this effect may provide a contrast mechanism for carrier-density mapping. On the other hand, in Figure 1c almost no difference is seen among high-N_{ZnO}, low-N_{ZnO} and dielectric samples at frequencies far away from ω_p. We shall then conduct s-SNOM experiments at two IR frequencies close to ω_p (ω_{IR1} ω_p and ω_{IR2} ω_p).

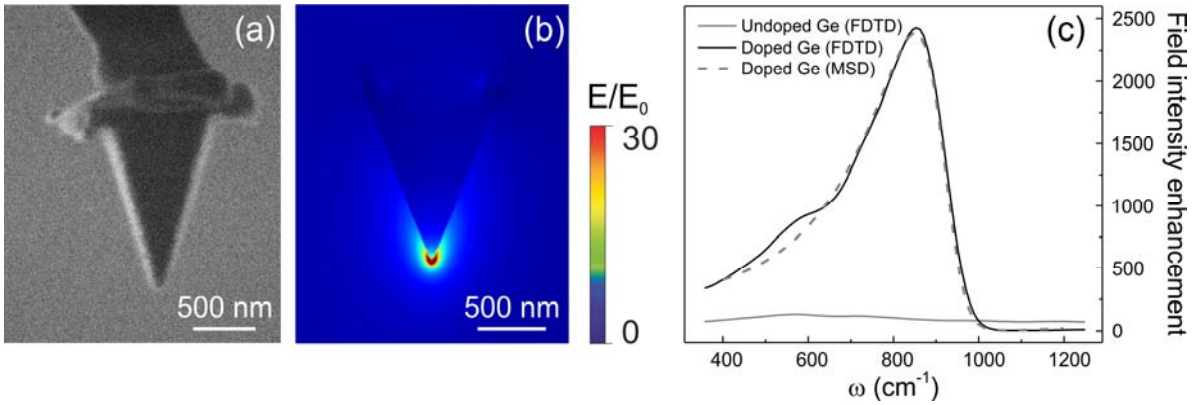

FIGURE 2. Doped semiconductor tip engineering. (a) Image of the engineered tip during nano-sculpturing of the pyramidal tip, taken with the focused ion beam at low ion currents. (b) Finite-Difference Time-Domain (FDTD) electromagnetic simulations of the electric field enhancement E/E_0 as a function of position in space at the peak enhancement frequency ω_{IR} = 850 cm^{-1}. (c) Field intensity enhancement $|E/E_0|^2$ as a function of ω_{IR} at a position 25 nm below the tip apex calculated with FDTD and with the multi-spherical dipole model described in the text. Simulations of doped Ge use the dielectric function of Figure 1a, those of undoped Ge use ε =16.0+0.001*i*.

We performed Finite Difference Time Domain (FDTD) simulations to estimate the plasmon resonance spectrum of the scanning probe tip used in this work, shown in Figure 2a. The tip is a n-Ge square-base pyramid with height of about 1.5 μm, side of about 1.0 μm and curvature radius of the tip apex $r \approx 50$ nm. The field enhancement map is reported in Figure 2b for ω_{IR} = 850 cm^{-1}. The electromagnetic field enhancement at the apex was calculated in Figure 2c (black solid line) as a function of ω_{IR} in the range 400-1250 cm^{-1} (λ ~ 8-25 μm) using illumination conditions identical to those of the s-SNOM experiment. The maximum field enhancement found at 850 cm^{-1} is clearly related to the resonant excitation of the free electron plasma in n-Ge, because it is absent when instead the dielectric function of undoped Ge ε=16.0+0.001*i* is considered (grey solid line in Figure 2c) [30]. It is then convenient to use the reliable CO_2 laser technology emitting at ω_{IR1} = 884 cm^{-1} in conjunction with a n-Ge tip with ω_p = 1050 cm^{-1}.

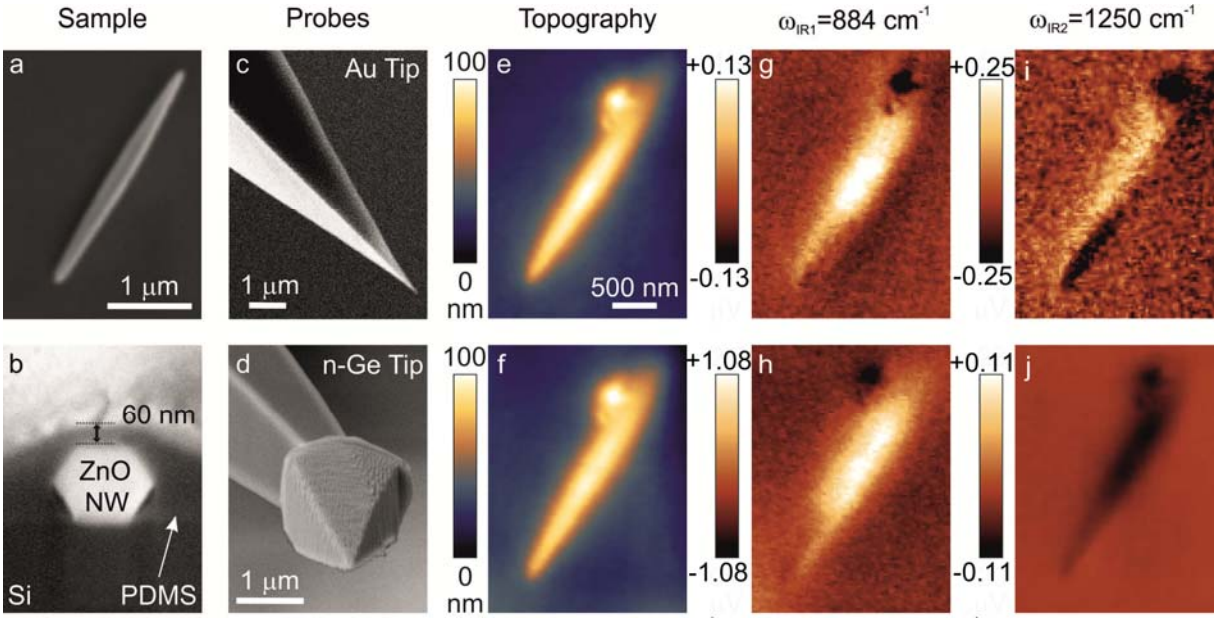

FIGURE 3. SNOM imaging of a nanowire. (a) SEM image of the ZnO nanowire dispersed on a silicon wafer. (b) Slice-and-view section of one of the NWs from the same sample buried under 60 nm of PDMS matrix. (c,d) SEM images of the gold-coated silicon tip (c) and of the n-Ge tip (d) used for mid-IR nanoimaging. (e,f) AFM topography of a selected NW on the test sample obtained with the two tips. (g-j) Maps of the s-SNOM signal $u_{(2)}$ taken at two different IR frequencies (884 and 1250 cm^{-1}) with the two tips. When imaged with the n-Ge tip (h,j), the nanowire displays contrast on the dielectric matrix of different sign at the two IR frequencies. Linear plane-fit was applied. In (i), a 2x2 Gaussian smoothing algorithm was also applied due to higher noise.

Near-field imaging experiment. We prepared a test sample made of doped ZnO NWs embedded in a polydimethylsiloxane (PDMS) matrix. Conductive-AFM measurements indicated that the different NWs have a large spread of conductivity values, and indeed in the hydrothermal crystal growth process the expected doping level varies widely in the range $N_{ZnO} \sim 10^{17}$-10^{20} cm^{-3} [15]. Figure 3a shows a SEM image of a single ZnO NW transferred onto a silicon substrate before blending it with PDMS, and Figure 3b shows the cross-section SEM image of another NW embedded in the same PDMS matrix. Embedding the NWs in a matrix is crucial for eliminating high topography steps that may impact on the scattering function producing artifacts in the s-SNOM maps [38, 39]. Also, there is an intrinsic technology interest in studying the conductivity of NWs embedded in a matrix because they form the building block of foldable nanophotonic and nanoelectronic devices [20, 21]. We used a commercial s-SNOM setup (Neasnom by Neaspec GmbH) where the doped semiconductor tip with ω_p = 1050 cm^{-1} is illuminated at grazing incidence with the electric-field vector oriented at an angle of 30° with respect to the surface normal. A mid-IR detector is aligned so as to measure the radiation intensity back-scattered in the far-field. The sample is scanned in the *x,y* plane and the detector output voltage $u(x,y)$ is measured [2]. The voltage u is proportional to the back-scattered light intensity that depends on the background (stray light) interfering with the near-field signal. The experimental near-field signal $u_{(i)}$ is therefore isolated by demodulation of the detector voltage at the i^{th}-harmonic of the cantilever tapping frequency Ω for $i \geq 2$, resulting in SNOM maps $u_{(i)}(x,y)$ like those demonstrated in Figures 3g-j for $i = 2$. The pseudo-heterodyne technique

described in Ref. 2, which allows direct retrieval of , could not be applied to the n-Ge tip, mainly because of increased mechanical noise of our nanoengineered probe if compared to monolithic scanning probes. This is attributed essentially to the weak mechanical link between the n-Ge pyramid and the silicon shaft, producing an increased noise power density at low modulation frequency below a few tens of kHz, which prevented the use, in the Neasnom microscope, of the Michelson interferometer with an oscillating mirror at around 300 Hz to demodulate the phase information [2]. Phase-stabilized homodyne SNOM [25, 26] or monolithic probe tip fabrication may represent a solution to this problem for future studies.

We imaged the NW of Figure 3a, of radius R_{NW} ~200 nm and buried under h ~ 60 nm of PDMS (see Figure 3b). Two IR lasers were used, one emitting at ω_{IR1} = 884 cm^{-1} < ω_p and one emitting at ω_{IR2} = 1250 cm^{-1} > ω_p. For direct comparison, the same NW was imaged with a gold-coated probe characterized by identical mechanical properties of the cantilever. The SEM images of the two probe tips are shown in Figures 3c-d. The respective AFM topography maps of the NW (Figures 3e-f) do not display significant differences between each other and they confirm the expected smooth variations of the topography. In the case of the gold-coated tip, the pseudo-heterodyne detection mode was applied. For simplicity, we focus on a specific location at the center of the NW, indicated in Fig. 4. The measurements of the s-SNOM intensity contrasts and phase shifts with respect to the PDMS background are shown in Figure 4a-b as black dots, and they are compared to the IPD model predictions with a gold-coated tip calculated for different free carrier parameters of the NW [10-11]. A free carrier density N_{ZnO} = 2.5·10^{19} cm^{-3} with an electron mobility of 25 cm^2/Vs gives a good fit to the data.

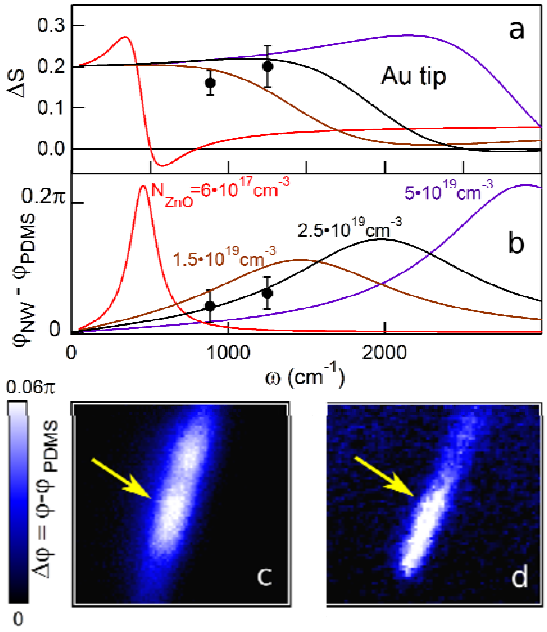

FIGURE 4. Scattering phase and amplitude measured with the gold-coated tip. (a, b) The scattering amplitude (a) and phase (b) contrast between a ZnO NW with different free carrier density calculated from the IPD model with a Au sphere of radius r = 50 nm (color curves) and measured in the pseudo-heterodyne detection mode (black dots, referring to the position at the NW center indicated by arrows in panels (c, d). The electron mobility values are the same as Figure 1c-d i.e. 62 cm^2/Vs for N_{ZnO} = 6·10^{17} cm^{-3} and 25 cm^2/Vs for the other curves. (c,d) Scattering phase contrast maps at 884 cm^{-1} (c) and 1250 cm^{-1} (d). The map size is 2×2 μm^2. The amplitude maps are reported in Figure 3g for 884 cm^{-1} and 3i for 1250 cm^{-1}. The formula used for the calculations in (a, b) is reported in the Supplemental Material, z = 70 nm was used.

In Figures 3g-j, the s-SNOM intensity maps $u_{(2)}(x,y)$ collected with either tip are shown for ω_{IR1} and ω_{IR2}. For each map, one can define the maximum experimental near-field contrast as:

$$\Delta u_{(i)} = \frac{u_{(i)}^{NW} - u_{(i)}^{PDMS}}{u_{(i)}^{PDMS}}, \qquad (2)$$

where $u_{(i)}^{NW}$ is measured at the center of the NW, and $u_{(i)}^{PDMS}$ is the average over the PDMS matrix surrounding the NW. The s-SNOM maps obtained with the gold-coated tip at ω_{IR1} and at ω_{IR2} both display a positive $\Delta u_{(2)}$ at the center of the NW that corresponds to the positive ΔS calculated in Figure 4a. Turning to the s-SNOM maps collected with the doped semiconductor tip, at $\omega_{IR1} < \omega_p$ a *positive* $\Delta u_{(2)} \approx +0.50$ is observed at the center of the NW (Figure 3h), while at $\omega_{IR2} > \omega_p$ a *negative* $\Delta u_{(2)} \approx -0.11$ is found (Figure 3j), demonstrating that the near-field interaction of the doped semiconductor tip with the ZnO NW is very different from that of the gold-coated tip. Understanding the precise reason for this difference requires electromagnetic modeling.

Electromagnetic model. The comparison between the experimental data of Figure 3 and the IPD model of Figure 1c must be done carefully, because in the present experiment with the n-Ge tip the scattering phase and amplitude could not be separately measured due to technical limitations of the nano-engineered tip explained above. Therefore the demodulated voltage signal at each frequency ω actually depends on the background amplitude $B_0(\omega)$ and phase $\phi_b(\omega)$, which are not related to the specific tip-sample interaction [2]:

$$u_{(i)}(\omega) \approx 2\kappa(\omega) B_0(\omega) \left|\tilde{S}(\omega)\right|_{(i)} \cos(\phi_b(\omega) - \phi_{s,(i)}(\omega)), \qquad (3)$$

where $\kappa(\omega)$ is the detector sensitivity. Now, B_0 can be considered as constant over the investigated area of size much smaller than λ, while ϕ_b smoothly varies with *x* and *y* because of the smooth topography variations of the PDMS matrix in which the NW is embedded. Also, from an inspection of Figure 1d, one should have a similar value of ϕ_s for both PDMS and the nanowire at each measurement frequency. Indeed, using doped semiconductor probe tip on weakly resonant samples results in a scattering phase variation with frequency driven by the tip and, as such, almost independent on the sample material. Within these approximations the cosine term in Equation 3 can be considered constant over each entire map (see Appendix), and the observed s-SNOM image contrasts $\Delta u_{(2)}$, almost entirely determined by the scattering amplitude, can now be compared with the IPD model calculation of the scattering intensity contrast $\Delta S = \left(\left|\tilde{S}^{NW}(\omega)\right|_{(i)} - \left|\tilde{S}^{PDMS}(\omega)\right|_{(i)}\right) / \left|\tilde{S}^{PDMS}(\omega)\right|_{(i)}$ where the values of $\left|\tilde{S}(\omega)\right|_{(i)}$'s are taken from the IPD model data for the doped semiconductor tip on a ZnO half-plane. Within the IPD model, at ω_{IR1} = 884 cm^{-1} the contrast ΔS is strong and positive for very high N_{ZnO}, weak and positive for very low N_{ZnO}. At ω_{IR} ~ 1250 cm^{-1}, a strong negative contrast is not expected for any N_{ZnO} value, and this is at clear odds with the observation of Figure 3j. To overcome this contradiction, it should be reminded that the IPD model may not be accurate enough to reproduce the s-SNOM contrast

determined by finite-size effects due to the nanostructured sample [40-43], to the engineered probe tip itself [28], or to both. In previous works that went beyond the IPD model, the scattering function of the tips was either calculated in the prolate spheroid approximation [41-46], or it was directly measured [28]. Here, instead, we simulate the n-Ge tip by using several n-Ge spheres of decreasing radii mimicking the decrease of the pyramid cross-section towards the tip apex. The number of spheres and their radii are selected in order to fit the near-field FDTD simulation data and to mimic the actual n-Ge tip geometry in Fig. 2(a): the smallest sphere has almost the same curvature radius, and the other spheres follow the pyramid angle. In comparison with the prolate spheroid approximation, both the finite size of the tip and the small curvature radius at the apex can be taken into account [44, 45]. Moreover, we simulate the ZnO NW by a further ZnO sphere embedded in a PDMS layer. All the spheres and the layers are considered in mutual polarization interaction, i.e. they are all affected by both the incident electric field and by the electric field radiated by the other spheres and layers. To do that, we employ a multiple-scattering code introduced in Ref. 47, which is a semi-analytical model and therefore its calculation is fast enough to provide the explicit dependences of the image contrast value with N_{ZnO} as a free parameter in the model. This multi-spherical dipole (MSD) model is here adapted to the doped Ge tip of the present experiments by choosing the four spheres of decreasing radii (240 nm, 120 nm, 60 nm, 30 nm) sketched in Figure 5a, a choice that nicely reproduces the shape of the tip as well as the FDTD resonance frequency spectrum (see the dashed line in Figure 2c) using the dielectric function $\varepsilon_{\mathrm{tip}}(\omega)$ given in Figure 1a. The fitting to the FDTD data and to the experimental results was achieved by considering only the dipole term in the multipole field expansion. We recall that, in the IPD model, the tip was modeled by a single sphere of radius r = 50 nm, and the FDTD spectrum of Figure 2c cannot be reproduced by a single sphere [37].

For the application of the MSD model to s-SNOM, we calculated the intensity of the backscattered radiation $\left|\tilde{E}_s\right|^2$ for many tip-sample distance values $z(t) = (z_{max}/2)(1 + \cos(\Omega\, t))$ reproducing tapping-mode operation of the probe ($z_{\max}$ ~ 100 nm). Then, the i^{th}-components of the t-dependent Fourier transform $\left|\tilde{E}_s\right|^2_{(i)}$ were computed for comparison with the experimental $u_{(2)}$ and $u_{(3)}$. The NW dielectric function includes N_{ZnO} as a free parameter. The sample is either considered as a 400 nm thick ZnO layer on a semi-infinite Si substrate (Figure 5a), or as a sphere of ZnO of 400 nm diameter embedded in PDMS and deposited on a semi-infinite Si substrate (Figure 5c), in order to directly assess the possible role of sample-related finite-size effects. For comparison with the experiment of Figure 3h and 3j, we calculated the s-SNOM intensity contrast of the buried NW over the PDMS matrix:

$$\Delta u^{calc}{}_{(i)}(\omega_{\mathrm{IR}}, N_{\mathrm{ZnO}}) = \frac{\left|\left|\tilde{E}_s^{\,ZnO}(\omega_{\mathrm{IR}}, N_{\mathrm{ZnO}})\right|^2_{(i)}\right| - \left|\left|\tilde{E}_s^{\,PDMS}(\omega_{\mathrm{IR}})\right|^2_{(i)}\right|}{E_0^2}, \qquad (4)$$

which is a real function of N_{ZnO} and ω_{IR}. In Figure 5b and 5d, the contrast for $i = 2$ is color-plotted as a function of N_{ZnO} and ω_{IR} for the two situations sketched in Figure 5a and 5c, respectively.

Looking at Figure 5b, one sees that the contrast $\Delta u^{calc}{}_{(2)}$ (homogeneous ZnO sample case) displays a clear imprint of the plasmon resonances of the n-Ge tip at 850 cm^{-1}, whose intensity increases for higher N_{ZnO} without any significant frequency shift. Also, for very low N_{ZnO} and for $\omega > \omega_p$, $\Delta u^{calc}{}_{(2)}$ is almost zero (areas of dark red color), and it even turns negative (areas of blue-green color), indeed matching the experimental observation of Figure 3j hence indicating that the effects due to the finite size of the tip, which are accounted for in the MSD model and not in the IPD model, cannot be neglected in the calculation of the total scattering function. The negative contrast for $\omega > \omega_p$ is not surprising, as scattering suppression was previously observed in s-SNOM performed with gold tips on the high-frequency side of vibrational [38, 40] or plasma [10] resonances of the sample. Here, instead, the resonance resides in the tip material, but it becomes more evident in the s-SNOM maps as N_{ZnO} increases (see Figure 5b). If one now adds the effect of the finite-size of the ZnO sample (Figure 5d), one sees that the overall picture is confirmed: at ω_{IR1} = 884 cm^{-1} one gets strong positive contrast for high N_{ZnO}, while at ω_{IR2} = 1250 cm^{-1} one instead gets weak negative contrast in the low 10^{19} cm^{-3} range of N_{ZnO}. Since Figure 5b and 5d are not fundamentally different at any $\omega_{IR} \leq 1250$ cm^{-1}, we derive that the sample-related finite-size effects are not significant in our experiments. Instead, at $\omega_{IR} > 1600$ cm^{-1} a clear difference between Figure 5b and 5d is observed in the bright spots for very high N_{ZnO} (top right corner of the color plots), which can indeed be tentatively assigned to sample-related finite-size effects becoming important for shorter wavelengths [40].

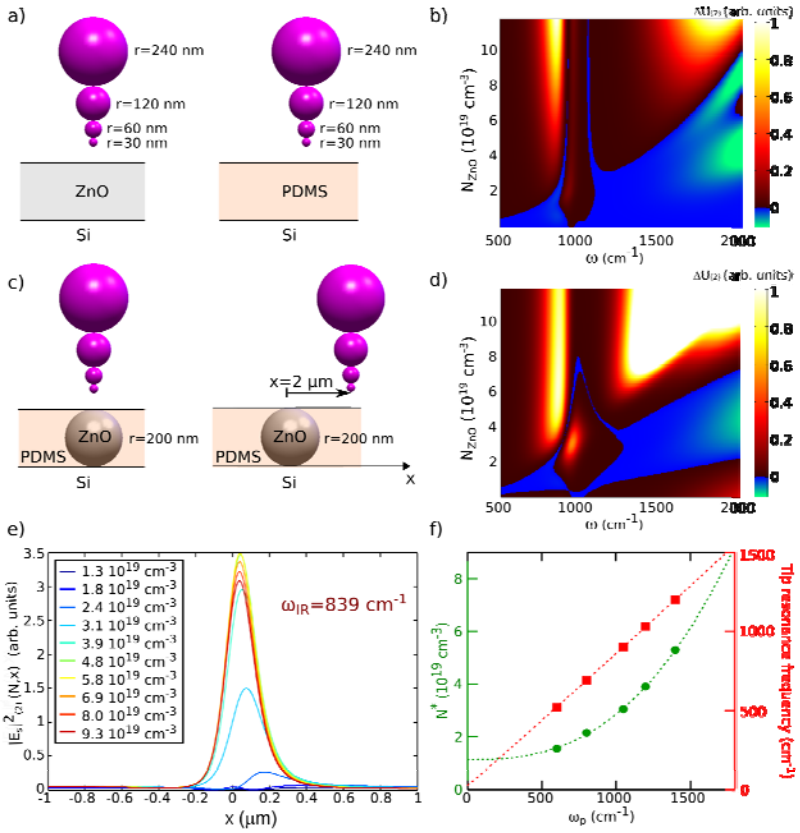

FIGURE 5. Multi spherical-dipole model of the s-SNOM experiment. (a) The scattering function of the engineered tip over a ZnO layer and over a PDMS layer, both on a Si substrate, is simulated by using four spheres of different radius for the Ge tip. (b) The calculated scattering intensity contrast $\Delta u^{calc}_{(2)}$ is color-plotted versus the values of ω_{IR} and N_{ZnO} (red-hot: positive contrast values; blue-green: negative contrast values). (c) The simulation is repeated by adding a ZnO sphere of radius R_{NW} = 200 nm representing a nanowire embedded in a PDMS matrix. The scattering intensity contrast was calculated for several displacements x of the n-Ge tip from the ZnO sphere and the zero-contrast condition (i.e. intensity identical to that of the geometry outlined on the right-hand side of panel (a)) was reproduced for $x > 2$ µm. The contrast $\Delta u^{calc}_{(2)}$ between x=0 µm and x=2 µm is then color-plotted in (d). (e) The scattering intensity for i=2 plotted vs. x for different values of N: the asymmetric s-SNOM profile of the ZnO sphere shows imprints of the illumination direction along x [41]. (f) A threshold carrier density N^* for NW visibility is defined from the data in (e) and from identical simulations where the plasma frequency ω_p of the n-Ge tip was varied (green dots). The plasmon resonance of the n-Ge tip is also plotted (red squares), dashed lines are guides to the eye. In all simulations, ε^{PDMS}=2.0, the n-Ge tip dielectric function is taken from Equation 1 and the Drude parameters other than N_{ZnO} used to reproduce the ZnO dielectric function are ε_∞ = 3.9, m*=0.29 m_e, γ=600 cm^{-1}. [23]

For an absolute evaluation of N_{ZnO} based on the MSD model of the experiment in Figure 3, we define a free carrier density threshold value N^* such that, for any $N_{ZnO} > N^*$, a ZnO NW becomes clearly visible in a transverse s-SNOM line-scan (see Figure 5e). For the n-Ge tip discussed in this work, one finds from the MSD model that $N^* \approx 2\times10^{19}$ cm^{-3}. The good visibility in Figure 3h of the NW with unknown N_{ZnO} implies that, therein, $N_{ZnO} > N^*$. The negative contrast observed at 1250 cm^{-1} (Figure 3j), globally compared to Figures 5b and 5d, suggest that N_{ZnO} should not approach ~ 10^{20} cm^{-3}. One can then provide a final estimate for N_{ZnO} in the low 10^{19} cm^{-3} range, which is in good agreement with the result ($N_{ZnO} \approx 2.5\cdot10^{19}$ cm^{-3}) obtained on the same NW with the gold-coated tip using the pseudo-heterodyne detection mode, shown in Figure 4. The noticeable feature of our engineered tips is that one could chose a tip material with ω_p optimized to be sensitive to different NW materials and carrier density ranges: Figure 5f shows the

plasmon resonance frequency of n-Ge probe tips, simulated within the MSD model, linearly scaling with ω_p. The corresponding value of N^*, also determined from the MSD model, has a super-linear but monotonic dependence on ω_p, indicating that engineered probe tips with high (low) ω_p will be more sensitive to the response of NWs with higher (lower) N_{ZnO}.

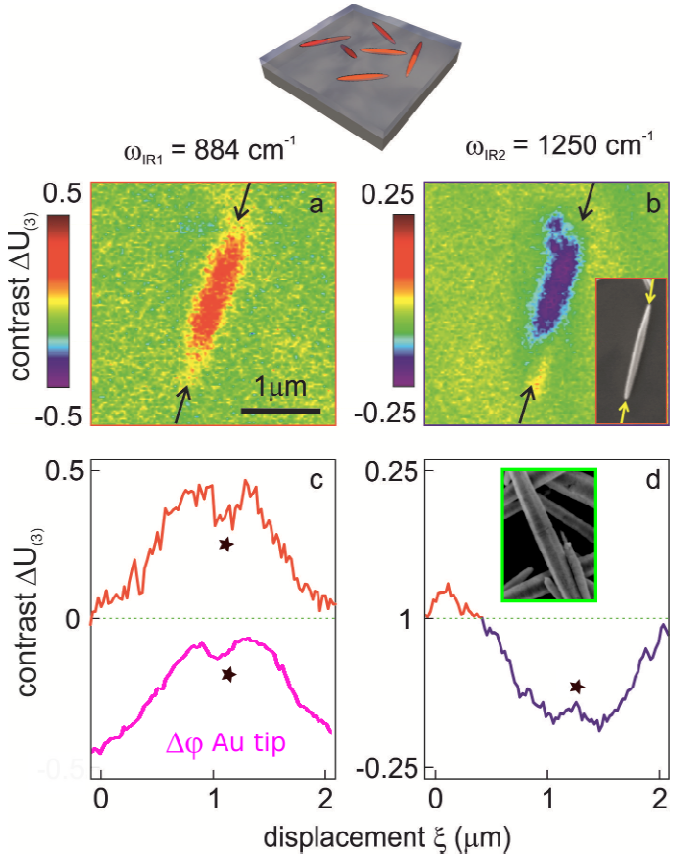

FIGURE 6. Assessment of the resolution of free-carrier profiling. (a-b) Maps of the SNOM contrast of a ZnO nanowire (NW) over the surrounding PDMS matrix observed at two IR frequencies. In the inset of (b) we show the SEM image of the same NW. (c-d) SNOM signal profile cuts between the two NW extremities indicated by the black arrows in (a,b) and by the yellow arrows in the inset of (b). The abscissa of (c,d) is the displacement coordinate ξ along the NW axis. The dashed green line represents the average value of the contrast observed on the surrounding PDMS matrix. The lower end of the NW (ξ < 0.5 μm) is buried under a larger thickness of PDMS and it is not visible in the present s-SNOM maps and profiles. The pink curve in panel (c) is the phase contrast profile measured with the gold-coated tip, extracted from Figure 4c. The pink curve is offset and scaled to match the red curve in the panel above. In panel (c), the higher noise level in the n-Ge tip profile (red curve) if compared to the Au tip (pink curve) is due to the higher mechanical noise of the nano-engineered tip. The stars in (c,d) correspond to a position with slightly lower carrier density in the NW. This feature is attributed to the initial growth seed of the NW, with higher crystal defect density. In the inset of panel (d), a SEM image of another similar NW is shown, where the initial growth seed position is seen as a transversal indent in the middle of the NW.

Imaging resolution of free carrier profiling. It has been recognized [19] that, beyond the absolute value of the conductivity, the free carrier-density profile in NWs is also extremely difficult to be reliably determined by contact-based methods. Non-contact optical methodologies have then been proposed, including Raman, photoluminescence and cathodoluminescence spectroscopy [48, 49]. Note that structural methodologies like secondary ion mass spectroscopy and atom probe only provide the density of dopant atoms, which may be very far from the actual free carrier density due to partial dopant activation [18]. Among optical methodologies, the approaches based on s-SNOM [6, 10, 11] directly provide the local free carrier density profile through determination of the Drude model parameters with sub-wavelength lateral resolution [10], which we demonstrate in the following also for our engineered doped semiconductor tips.

In Figure 6 the maps and the line profiles along the NW axis of the near-field signal are shown for ω_{IR1} and ω_{IR2}. Therein, the signal $u_{(3)}$ is plotted instead of $u_{(2)}$, because $u_{(3)}$ has weaker background interference and is therefore

better suited for a quantitative analysis [50]. Figure 6a displays the s-SNOM image taken at ω_{IR1} where the NW has high positive image contrast, as already seen in Figure 3h for the $u_{(2)}$ map. Line profiles measured across the NW for different positions along the axis [27, 37] indicate a s-SNOM lateral resolution of 100±20 nm at both λ_{IR1}=11.3 μm and λ_{IR2}=8.0 μm hence ~λ/100. The lateral resolution is only slightly broader than both the embedding depth $h \sim 70$ nm and the radius of curvature $r \sim 50$ nm, as typically obtained in the s-SNOM imaging of buried nanostructures [8]. The s-SNOM line profile at ω_{IR1} along the NW axis (oblique coordinate ξ, Figure 6c) shows a high signal in the central portion of the NW, almost constant with ξ, and a slow decrease towards the NW ends. At ω_{IR2} (Figure 5b and 5d), again the NW shows a negative image contrast as in Figure 3j but the signal-to-noise ratio is even better than that at ω_{IR1}. The slow decrease of the scattering contrast from ξ=0.5 μm to ξ=0.1 μm, and then from ξ=1.2 μm to ξ=1.5 μm, in both Figure 6c and 6d, is probably due to the increasing h or the decreasing R_{NW} value towards the ends of the NW (see the cigar-like shape of the NW in Figure 3a), both impacting on the strength of the near-field interaction of the doped semiconductor tip with the NW [50-52]. Importantly, the profile of the phase shift measured with the gold-coated tip, extracted from the phase map in Figure 4c and reported in Figure 6c with an offset, displays exactly the same features as the intensity profiles measured with the n-Ge tip, confirming that the profile variations at constant h and R_{NW} in the central portion of the NW (from ξ=0.5 μm to ξ=1.2 μm) are likely due to free carrier density variations. A constant N_{ZnO} is found along the NW axis, apart from a dip at the position around ξ=0.8 μm, marked by stars in Figure 6c and 6d, which points towards a local depletion of the free carriers, perhaps due to the presence of a structural nucleation defect like the one visible in the inset of Figure 6c. This type of nucleation defects often correlates to local suppression of the free carrier density in ZnO NWs grown with the hydrothermal method [53]. We notice that the signal decrease at the NW ends and the dip at ξ=0.8 μm is identically seen at both ω_{IR1} and ω_{IR2}, independently on the sign of the image contrast (positive for $\omega_{IR1} < \omega_p$ and negative for $\omega_{IR2} > \omega_p$), confirming that the doped semiconductor tip presented in this work features clear near-field interactions with the sample, both above and below its plasma frequency ω_p, and is able to capture small local variations in N_{ZnO}.

CONCLUSIONS

Scanning near-field optical microscopy has been performed with purposely engineered doped semiconductor tips featuring a plasma frequency in the mid-infrared range. The intrinsic plasma resonance in the tip material (epitaxial heavily electron-doped germanium) provided a strongly wavelength-dependent scattering intensity contrast displaying a clear correlation with the free carrier density in ZnO nanowires with a very short Drude relaxation time. The free carrier density range of a single ZnO nanowire could be estimated by comparing the image contrast of the near-field microscopy maps acquired at two wavelengths, one above and one below the plasma wavelength of the tip, to the image

contrast calculated using a semi-analytic multi-spherical dipole model of the near-field microscopy experiment. The results are positively benchmarked against those obtained with a conventional gold-coated tip in the more precise pseudo-heterodyne detection mode, where both phase and amplitude are measured. The model has also clarified that the shape and size of the doped semiconductor tip strongly affect the scattering image contrast, while the shape and size of the nanowire have a lower impact. Our doped semiconductor tips therefore provide the same kind of information as that provided by the commonly used gold-coated tips for specific s-SNOM experiments. In the future, the monolithic fabrication of scanning probes made of epitaxial material layers may open new avenues in near-field optical microscopy and scanning probe microscopy in general.

APPENDIX

Scanning probe tips made of doped semiconductors are fabricated by modifying commercial visible-apex silicon probes (Nanosensors ATEC-NC) as described in Video 1. These tips had been previously used to perform AFM topography imaging in contact and tapping mode, micro-photoluminescence emission, and s-SNOM tests [27]. The epitaxial germanium layers used in this work are grown on silicon wafers by plasma-enhanced chemical vapor deposition using GeH_4 and PH_3 as gas precursors. A 2 µm-thick undoped Ge buffer layer is followed by the growth of a 2 µm-thick electron-doped n-Ge layer with reduced defect density. The activated doping level $n \approx 2.5\times10^{19}$ cm^{-3} is determined by Hall transport measurements [29]. Heavily electron-doped germanium has $m^* = 0.12\ m_e$, $\varepsilon_\infty = 16$ and with these values the plasma frequency can be predicted from the free carrier density from $\omega_p^2 = n/m^*\varepsilon_\infty$. Heavily doped n-Ge films can nowadays be epitaxially grown in few-µm thick layers perfectly suited for the fabrication of scanning probe tips, and the value of ω_p can be widely tuned in the mid-IR range up to about 2500 cm^{-1}, as verified by IR spectroscopy on different semiconductor wafers [29].

Electromagnetic simulations are conducted using a commercial software (Lumerical Inc. FDTD Solutions v8.9 software) for the FDTD data in Figure 2 and with a home-made code for Green's function formalism [37] for the MSD data in Figure 5 [51]. The NW dielectric function was calculated from the Drude model with parameters suitable for ZnO: m^*=0.29 m_e , ε_∞ =3.7 and different values of N in the 10^{17}-10^{20} cm^{-3} range. Illumination conditions replicated the Neaspec reflective objective at grazing incidence, with 90 degree total horizontal opening angle, 20 degree vertical opening angle, and 60 degree incidence angle.

ZnO nanowires are grown by the hydrothermal method at 90 °C in an equimolar aqueous solution (5mM) of $Zn(NO_3)_2{\cdot}6H_2O$ and $C_6H_{12}N_4$. Nanowires are immersed in a liquid solution of polydimethylisiloxane (PDMS) diluted 1:40 in n-heptane, which is then spun at 5000 rpm onto silicon wafers and thermally cured on hotplate at 80 °C to form a conformal elastomeric matrix (thickness ranging from ~60 nm on top of the NWs to 180 nm in the empty matrix areas).

s-SNOM is performed with a scanning-sample AFM where the tip is illuminated with a focused laser beam (Neasnom by Neaspec GmbH). The laser systems employed in this work are a CO_2 gas laser at 884 cm^{-1}, and a quantum cascade laser with emission at 1250 cm^{-1}. The detector of the back-scattered radiation is a liquid nitrogen-cooled HgCdTe photovoltaic sensor. The scattered intensity signals $u_{(2)}$, $u_{(3)}$ are amplified by lock-in demodulation at 2Ω and 3Ω, in order to isolate the contribution due to the near-field tip-sample interaction (Ω ~ 70 kHz, cantilever chips by Nanosensors, model ATEC-NC). Measurement on test samples conducted with

the n-Ge tip demonstrated the near-field nature of the signal [37]. In order to maximize the s-SNOM contrast, the collection optics was aligned with the tip on a position far from the NW, and ϕ_B was set to smoothly vary around values close to 0 (i.e. the cosine term in Equation 3 was maximized to smoothly vary around a value close to 1, considering that $\phi_S \cong 0$ on the weakly absorbing PDMS matrix). In this way, the problem of low-frequency mechanical noise of the n-Ge tip that prevented pseudo-heterodyne detection was partly circumvented. The pseudo-heterodyne detection was instead performed with a gold-coated Nanosensors ATEC-NC tip, with the Michelson interferometer built into the Neasnom microscope, with the moving mirror oscillating at 300 Hz.

Ackowledgements. The authors acknowledge support from Andreas Huber of Neaspec GmbH, and wish to thank Shaul Aloni, Virginia Altoe, Luca Businaro, Adele De Ninno and Michele Celebrano for technical help. The work was partly funded by the Italian Ministry of Research through programs FIRB Futuro in Ricerca (Grant No. RBFR08N9L9) and SIR (Grant No. RBSI14IT0D). The research leading to these results has also received funding from the European Union's Seventh Framework Programme under grant agreement n°613055. Work at the Molecular Foundry was supported by the Office of Science, Office of Basic Energy Sciences, of the U.S. Department of Energy under Contract No. DE-AC02-05CH11231, Molecular Foundry User Proposal no. 1773.

Supplemental Material include: (1) a video on the scanning probe tip nanofabrication process; (2) a description of the application of the MSD model to s-SNOM; (3) quantitative evaluation of the lateral resolution of s-SNOM with engineered semiconductor tips; (4) Figure 3 with the absolute values of signal intensities; (5) experiments on test samples (homogeneous Si and doped Ge films).

References

1. F. Keilmann and R. Hillenbrand, Near-field Microscopy by Elastic Light Scattering from a Tip, *Philos. Trans. R. Soc. London Ser. A* **362**, 787 (2004).
2. N. Ocelic, A. Huber, and R. Hillenbrand. Pseudoheterodyne Detection for Background-Free Near-Field Spectroscopy, *Appl. Phys. Lett.* **89**, 101124, (2006).
3. M. M. Qazilbash, M. Brehm, B. G. Chae, P. C. Ho, G. O. Andreev, B. J. Kim, S. J. Yun, A. V. Balatsky, M. Maple, F. Keilmann, H. T. Kim, and D. N. Basov, Mott Transition in VO_2 Revealed by Infrared Spectroscopy and Nano-imaging, *Science* **318**, 1750 (2007).
4. A. J. Huber, F. Keilmann, J. Wittborn, J. Aizpurua, and R. Hillenbrand, Terahertz Near-Field Nanoscopy of Mobile Carriers in Single Semiconductor Nanodevices, *Nano Lett.* **8**, 3766 (2008).
5. E. A. Muller, B. Pollard, H. A. Bechtel, P. Van Blerkom and M. B. Raschke, Infrared Vibrational Nanocrystallography and Nanoimaging, *Science Advances* **2**, e1601006 (2016).
6. M. Eisele, T. L. Cocker, M. A. Huber, M. Plankl, L. Viti, D. Ercolani, L. Sorba, M. S. Vitiello, and R. Huber, Ultrafast multi-terahertz nano-spectroscopy with sub-cycle temporal resolution, *Nature Photon.* **8**, 841 (2014).
7. Z. Shi, X. Hong, H. A. Bechtel, B. Zeng, M. C. Martin, K. Watanabe, T. Taniguchi, Y. Shen, and F. Wang, Observation of a Luttinger-liquid plasmon in metallic single-walled carbon nanotubes, *Nature Photon.* **9**, 515, (2015).
8. M. Wagner, A. S. McLeod, S. J. Maddox, Z. Fei, M. Liu, R. D. Averitt, M. Fogler, S. R. Bank, F. Keilmann, and D. N. Basov, Ultrafast Dynamics of Surface Plasmons in InAs by Time-Resolved Infrared Nanospectroscopy, *Nano Lett*. **14**, 4529 (2014).
9. J. M. Atkin, S. Berweger, A. C. Jones, and M. B. Raschke, Nano-optical Imaging and Spectroscopy of Order, Phases, and Domains in Complex Solids, *Advances in Physics* **61**, 745 (2012).
10. J. M. Stiegler, A. J. Huber, S. L. Diedenhofen, J. Gómez Rivas, R. E. Algra, E. P. A. M. Bakkers, and R. Hillenbrand, Nanoscale Free-Carrier Profiling of Individual Semiconductor Nanowires by infrared Near-Field Nanoscopy, *Nano Lett.* **10**, 1387 (2010).
11. J. M. Stiegler, R. Tena-Zaera, O. Idigoras, A. Chuvilin, and R. Hillenbrand, Correlative infrared–electron nanoscopy reveals the local structure–conductivity relationship in zinc oxide nanowires. *Nature Commun.*, **3**, 1131 (2013).
12. X. Duan, Y. Huang, Y. Cui, J. Wang, and C. M. Lieber, Indium Phosphide Nanowires as Building Blocks for Nanoscale Electronic and Optoelectronic Devices, *Nature* **409,** 66 (2001).
13. D. Saxena, S. Mokkapati, P. Parkinson, N. Jiang, Q. Gao, H. H. Tan, and C. Jagadish, Optically Pumped Room-temperature GaAs Nanowire Lasers, *Nature Photon.*, **7**, 963 (2013).
14. X. Yang, A. Wolcott, G. Wang, A. Sobo, R. C. Fitzmorris, F. Qian, J. Z. Zhang and Y. Li, Nitrogen-Doped ZnO Nanowire Arrays for Photoelectrochemical Water Splitting, *Nano Lett.* **9**, 2331 (2009).
15. A. Janotti and C. G. Van de Walle, Fundamentals of zinc oxide as a semiconductor, *Reports on Progress in Physics* **72**, 126501 (2009).
16. E. C. Garnett, Y. Tseng, D. R. Khanal, J. Wu, J. Bokor and P. Yang, Dopant profiling and surface analysis of silicon nanowires using capacitance-voltage measurements, *Nature Nanotechnol.* **4**, 311 (2009).

17. E. Koren, N. Berkovitch, and Y. Rosenwaks, Measurement of active dopant distribution and diffusion in individual silicon nanowires. *Nano Lett.* **10**, 1163 (2010).
18. J. E. Allen, D. E. Perea, E. R. Hemesath and L. J. Lauhon, Nonuniform Nanowire Doping Profiles Revealed by Quantitative Scanning Photocurrent Microscopy, *Adv. Mater.* **21**, 3067 (2009).
19. H. J. Joyce, J. Boland, C. L. Davies, S. A. Baig, and M. B. Johnston, A review of the electrical properties of semiconductor nanowires: insights gained from terahertz conductivity spectroscopy, *Semicond. Sci. Technol.* **31**, 103003 (2016).
20. D. Vanmaekelbergh and L. K. Van Vugt, ZnO Nanowire Laser, *Nanoscale* **3**, 2783 (2011).
21. Z. L.Wang and J. Song, Piezoelectric Nanogenerators Based on Zinc Oxide Nanowire Arrays, *Science* **312**, 242 (2006).
22. Th. P. H. Sidiropoulos, R. Roder, S. Geburt, O. Hess, S. A. Maier, C. Ronning, and R. F. Oulton, Ultrafast plasmonic nanowire lasers near the surface plasmon frequency, *Nature Phys.* **10**, 870 (2014).
23. J. B. Baxter and C. Schmuttenmaer, Conductivity of ZnO Nanowires Nanoparticles and Thin Films Using Time-Resolved Terahertz Spectroscopy, *J. Phys. Chem. B* **110**, 25229 (2006).
24. S. Kalusniak, S. Sadofev and F. Henneberger, ZnO as a Tunable Metal: New Types of Surface Plasmon Polaritons, *Phys. Rev. Lett.* **112**, 137401 (2014).
25. X. G. Xu, L. Gilburd, and G. C. Walker, Phase Stabilized Homodyne of Infrared Scattering Type Scanning Near-Field Optical Microscopy. *Appl. Phys. Lett.* **105**, 263104 (2014).
26. X. G. Xu, A. E. Tanur and G. C. Walker, Phase Controlled Homodyne Infrared Near-Field Microscopy and Spectroscopy Reveal Inhomogeneity Within and Among Individual Boron Nitride Nanotubes. *J. Phys. Chem. A* **117**, 3348–3354 (2013).
27. V. Giliberti, E. Sakat, M. Bollani, M. V. P. Altoe, M. Melli, A. Weber-Bargioni, L. Baldassarre, M. Celebrano, J. Frigerio, G. Isella, S. Cabrini and M. Ortolani, Functionalization of Scanning Probe Tips with Epitaxial Semiconductor Layers, *Small Methods* **1,** 1600033 (2017).
28. F. Huth, A. Chuvilin, M. Schnell, I. Amenabar, P. Krutokhvostov, S. Lopatin, and R. Hillenbrand, Resonant Antenna Probes for Tip-Enhanced infrared Near-Field Microscopy, *Nano Lett.* **13**, 1065 (2013).
29. J. Frigerio, A. Ballabio, G. Isella, E. Sakat, G. Pellegrini, P. Biagioni, M. Bollani, E. Napolitani, C. Manganelli, M. Virgilio, A. Grupp, M. P. Fischer, D. Brida, K. Gallacher, D. J. Paul, L. Baldassarre, P. Calvani, V. Giliberti, A. Nucara, and M. Ortolani, Tunability of the dielectric function of heavily doped germanium thin films for mid-infrared plasmonics, *Phys. Rev. B* **94**, 085202 (2016).
30. L. Baldassarre, E. Sakat, J. Frigerio, A. Samarelli, K. Gallacher, E. Calandrini, G. Isella, D. J. Paul, M. Ortolani, and P. Biagioni, Midinfrared Plasmon-Enhanced Spectroscopy with Germanium Antennas on Silicon Substrates, *Nano Lett.* **15**, 7225 (2015).
31. M. Fleischer, A. Weber-Bargioni, M. V. P. Altoe, A. Schwartzberg, P. J. Schuck, S. Cabrini and D. P. Kern, Gold Nanocone Near-Field Scanning Optical Microscopy Probes, *ACS Nano* **5**, 2570 (2011).
32. T. W. Johnson, Z. J. Lapin, R. Beams, N. C. Lindquist, S. G. Rodrigo, L. Novotny and S. H. Oh, Highly Reproducible Near-Field Optical Imaging with Sub-20-nm Resolution Based on Template-Stripped Gold Pyramids, *ACS Nano* **6**, 9168 (2012).
33. F. De Angelis, G. Das, P. Candeloro, M. Patrini, M. Galli, A. Bek, M. Lazzarino, I. Maksymov, C. Liberale, L. C. Andreani and E. Di Fabrizio, Nanoscale Chemical Mapping Using Three-Dimensional Adiabatic Compression of Surface Plasmon Polaritons, *Nature Nanotechnol.***5**, 67 (2010).
34. W. Bao, M. Melli, N. Caselli, F. Riboli, D. S. Wiersma, M. Staffaroni, H. Choo, D. F. Ogletree, S. Aloni, J. Bokor, S. Cabrini, F. Intonti, M. B. Salmeron, E. Yablonovitch, P. J. Schuck, and A. Weber-Bargioni, Mapping local charge recombination heterogeneity by multidimensional nanospectroscopic imaging, *Science* **338**, 1317 (2012).
35. V. Giliberti, E. Sakat, L. Baldassarre, A. Di Gaspare, A. Notargiacomo, E. Giovine, J. Frigerio, G. Isella, M. Melli, A. Weber-Bargioni, S. Aloni, S. Sassolini, S. Cabrini, P. Biagioni, M. Ortolani and M. Bollani, Three-dimensional fabrication of free-standing epitaxial semiconductor nanostructures obtained by focused ion beam, *Microelectron. Eng.*, **141**, 168 (2015).
36. Y. Zou, P. Steinvurzel, T. Yang, and K. B. Crozier, Surface Plasmon Resonances of Optical Antenna Atomic Force Microscope Tips, *Appl. Phys. Lett.* **94**, 171107 (2009).
37. See Supplemental Material at [URL will be inserted by publisher] for the dipole model formula, the details on the model comparison and the lateral resolution of s-SNOM with the n-Ge tip.
38. M. Brehm, T. Taubner, R. Hillenbrand and F. Keilmann, Infrared Spectroscopic Mapping of Single Nanoparticles and Viruses at Nanoscale Resolution, *Nano Lett.* **6**, 1307 (2006).
39. J. J. Greffet, A. Sentenac and R. Carminati, Surface Profile Reconstruction Using Near-Field Data, *Opt. Commun*. **116**, 20 (1995).
40. J. M. Stiegler, Y. Abate, A. Cvitkovic, Y. E. Romanyuk, A. J. Huber, S. R. Leone, and R. Hillenbrand, Nanoscale Infrared Absorption Spectroscopy of Individual Nanoparticles Enabled by Scattering-Type Near-Field Microscopy, *ACS Nano* **5**, 6494 (2011).
41. R. Esteban, R.Vogelgesang, and K. Kern, Full Simulations of the Apertureless Scanning Near Field Optical Microscopy Signal: Achievable Resolution and Contrast. *Opt. Express* **17**, 2518 (2009).
42. Z. H. Kim and S. H Ahn, Nanometer-Scale Dielectric Imaging of Semiconductor Nanoparticles: Size-Dependent Dipolar Coupling and Contrast Reversal, *Nano Lett.* **7**, 2258 (2007).
43. M. Esslinger and R. Vogelgesang, Reciprocity Theory of Apertureless Scanning Near-Field Optical Microscopy with Point-Dipole Probes, *ACS Nano*, **6**, 8173 (2012).
44. A. Cvitkovic, N. Ocelic, and R. Hillenbrand, Analytical Model for Quantitative Prediction of Material Contrasts in Scattering-Type Near-Field Optical Microscopy, *Opt. Express* **15**, 8550 (2007).
45. A. S. McLeod, P. Kelly, M. D. Goldflam, Z. Gainsforth, A. J. Westphal, G. Dominguez, M. H. Thiemens, M. M. Fogler, and D. N. Basov, Model for quantitative tip-enhanced spectroscopy and the extraction of nanoscale-resolved optical constants, *Phys. Rev. B* **90**, 085136 (2014).

46. B.-Y. Jiang, L. M. Zhang, A. H. Castro Neto, D. N. Basov, and M. M. Fogler, Generalized spectral method for near-field optical microscopy, *J. Appl. Phys.* **119**, 054305 (2016).
47. M. Langlais, J. P. Hugonin, M. Besbes, and P. Ben-Abdallah, Cooperative electromagnetic interactions between nanoparticles for solar energy harvesting, *Opt. Express* **22**, A577 (2014).
48. D. Lindgren, O. Hultin, M. Heurlin, K. Storm, M. T. Borgström, L. Samuelson, and A. Gustafsson, Study of carrier concentration in single InP nanowires by luminescence and Hall measurements, *Nanotechnology* **26**, 045705 (2015).
49. B. Ketterer, E. Uccelli, and A. Fontcuberta i Morral, Mobility and carrier density in p-type GaAs nanowires measured by transmission Raman spectroscopy, *Nanoscale* **4**, 1789 (2012).
50. A. A. Govyadinov, S. Mastel, F. Golmar, A. Chuvilin, P. S. Carney, and R. Hillenbrand, Recovery of Permittivity and Depth from Near-Field Data as a Step toward Infrared Nanotomography, *ACS Nano* **8**, 6911 (2014).
51. G. Wollny, E. Bründermann, Z. Arsov, L. Quaroni, and M. Havenith, Nanoscale depth resolution in scanning near-field infrared microscopy. *Opt. Express* **16**, 7453 (2008).
52. A. P. Engelhardt, B. Hauer and T. Taubner, Visibility of weak contrasts in subsurface scattering near-field microscopy. *Ultramicroscopy* **126**, 40 (2013).
53. Y. F. Hsu, Y. Y. Xi, K. H. Tam, A. B. Djurišić, J. Luo, C. C. Ling, C. K. Cheung, A. M. C. Ng, W. K. Chan, X. Deng, C. D. Beling, S. Fung, K. W. Cheah, P. W. K. Fong, and C. C. Surya, Undoped p-Type ZnO Nanorods Synthesized by a Hydrothermal Method, *Adv. Funct. Mater.* **18**, 1020 (2008).